Nano Energy 89 (2021) 106337

Contents lists available at ScienceDirect

Nano Energy

journal homepage: www.elsevier.com/locate/nanoen

Harnessing artificial intelligence to holistic design and identification for solid electrolytes

Zhilong Wang [a], Xirong Lin [a], Yanqiang Han [a], Junfei Cai [a], Sicheng Wu [a], Xing Yu [b], Jinjin Li [a,*]

[a] Key Laboratory of Thin Film and Microfabrication Technology, Ministry of Education, Shanghai Jiao Tong University, Shanghai 200240, China
[b] Key Laboratory of Submarine Geosciences & Second Institute of Oceanography, Ministry of Natural Resources, Hangzhou 310012, China

ARTICLE INFO

Keywords:
Lithium-ion batteries
Solid-state batteries
Solid electrolytes
Artificial intelligence
Garnet materials

ABSTRACT

Despite extensive studies, the development of solid-state batteries (SSBs) has not yet met expectations, owing mainly to the lack of suitable solid electrolytes (SEs) that exhibit low electronic conductivity (σ_e), high ionic conductivity (σ_i), and good stability. Here, we propose an effective target-driven framework for holistic identifying promising garnet-type SEs. Using artificial intelligence (AI) technologies, we accurately predict the σ_e with a mean absolute error of 0.25 eV, achieving a computed speed that is $\sim 10^9$ faster than ab initio calculations. Successfully, from 29,008 garnets, we discovered 12 promising super Li-ion conductors for SEs with $\sigma_e < 3.6 \times 10^{-30}$ S cm^{-1}, $\sigma_i > 10^{-4}$ S cm^{-1} (up to 3.24 S cm^{-1}), and good thermal stability at room temperature and high temperature based on rigorous ab initio validation. These emerging SEs are expected to be used in Li-ion SSBs, thus improving the safety, performance, and lifetime of state-of-the-art energy storage technology. This approach directly cuts across at least 95 years of computational cycles to screen SEs, resulting in significant cost savings and helping us enter an electrified future that relies less on fossil fuels.

Data availability: The data that support the machine learning model of this study are available at: https://www.materialsproject.org.

1. Introduction

Lithium-ion batteries (LIBs), as representative modern high-performance batteries, are widely used in our lives in devices ranging from personal electronics and electric vehicles (EVs) to aerospace devices [1–3]. However, traditional LIBs employ flammable liquid electrolytes, suffer from insufficient energy density and lithium dendrite issues and pose potential safety risks (spontaneous combustion and explosion) [4,5]. Advanced energy storage technologies urgently need to be developed considering the rapid growth of electric vehicles and grid energy storage demands, leading to significant attention that has been paid to achieving higher energy density, better safety, and lower expenditure for battery equipment [6–8]. Although liquid electrolytes have high ionic conductivity and good electrode wettability, the diversity and complexity of electrolyte components (including salts, organic or inorganic solvents and additives) inevitably present many challenges, which are closely related to their uncontrollable constituents [9]. Therefore, we are motivated to explore beyond traditional LIB technologies (such as solid-state aluminum-ion batteries (AIBs) [10–12], sodium-ion batteries (SIBs) [13–15], magnesium-ion batteries (MIBs) [16,17]), and the design or discovery of solid electrolytes (SEs) [18–20]. In particular, due to the high mechanical strength and noninflammable nature of SEs, solid-state batteries (SSBs) hopefully completely address the safety and dendrite issues of LIBs and achieve high energy density with low-cost manufacturing technology [21,22]. Consequently, designing and finding excellent SEs is regarded as one of the critical challenges and has continued to attract enormous attention over recent years [18,23].

The best SE materials must have high ionic conductivity ($\sigma_i > 10^{-4}$ S cm^{-1}, or "superionic conductors"), low electronic conductivity ($\sigma_e < 3.6 \times 10^{-30}$ S cm^{-1}, or band gap > 4.0 eV, insulating), and good thermal stability at room temperature (R_T) [18,24,25]. σ_i is a key factor in determining the internal resistance and multiplier performance of the battery. When the electrolyte σ_i is high, insulation treatment (low σ_e) should be carried out to ensure that the electron across the electrolyte is negligible, avoiding the occurrence of a self-discharge process [18]. In particular, Han et al. revealed that lithium dendrites are more likely to form in solid electrolytes because of the high electronic conductivity of solid electrolytes [25]. With such stringent criteria, most of the currently well-studied SEs may be excluded due to the difficulty of meeting all the

* Corresponding author.
E-mail address: lijinjin@sjtu.edu.cn (J. Li).

https://doi.org/10.1016/j.nanoen.2021.106337
Received 22 April 2021; Received in revised form 29 May 2021; Accepted 10 July 2021
Available online 14 July 2021

conditions, and the low ion mobility is usually neglected in most research work. Although a great deal of work has been done on various aspects of SE research, determining which electrolyte is more suitable for SSB applications is still a great challenge. Perovskite-type SE $Li_{3x}La_{2/3-x}Ø_{1/3-2x}TiO_3$ (Ø, vacancy, $0 < x < 0.16$) (LLTO) shows a high bulk σ_i of 10^{-3} S cm^{-1} at R_T, but the conductivity is greatly affected by the crystal lattice and relative lithium concentration [26,27]. $Li_xPO_yN_z$ ($x = 2y + 3z - 5$) (LiPON) has good stability but exhibits a low σ_i of 10^{-6} S cm^{-1}. $Li_{14}ZnGe_4O_{16}$ (LZGO, LISICON-type) exhibits a γ-Li_3PO_4-type structure with a high σ_i of ~0.125 S cm^{-1} at 600 K, but it decreases sharply to ~10^{-7} S cm^{-1} at R_T [28]. Among the different types of SEs, garnet-type $Li_7La_3Zr_2O_{12}$ (LLZO), with a relatively high σ_i of 10^{-4}–10^{-3} S cm^{-1}, good stability, and large electrochemical window, has been considered one of the most promising and important SEs [29]. The question of whether the σ_i can be further improved is also still open. Recent studies on the ionic conductivity, electronic conductivity, synthesis, and battery architectures of garnet-type SEs have been reported extensively [30,31]. Designing and seeking ideal garnet-type SEs has become the focus of current researchers. However, to date, there has not been a systematic mining of garnet materials for SEs.

Conventional garnet materials are a group of orthosilicates that have a common chemical formula of $\{A\}_3(B)_2[C]_3\langle X\rangle_{12}$ (A, B, and C cations occupy eight, six, and four coordination sites, respectively, and X anions occupy vertices) and crystallize in a cubic structure (space group $Ia\bar{3}d$). There are vast selections for A-, B- and C-sites such as A = Ca, Mg, Na, La, B = Al, Fe, Ga, Sc, and C = Si, Ge, Al, Li, combining into tens of thousands of different garnets. When A-, B-, or C-sites within garnet structures are occupied by Li, Mg, Al, etc., they become potentially garnet-type SEs for LIBs, MIBs, AIBs, etc. Both experimental and computational methods contribute to the targeted exploration of garnet-type SEs; in particular, first-principles calculations based on density functional theory (DFT) can provide microscopic viewpoints on atomic shuttles, lattice distortion, and thermal dynamic stability [30,32]. However, in the vast search space for garnet materials, these traditional approaches are not suitable for such a huge screening and discovery process, which will undoubtedly produce huge costs and will be time-consuming. For this main reason, garnet-type SEs have so far not been studied on a large scale. Gratifyingly, with the rapid development of material informatics, DFT calculations integrate many machine learning (ML) algorithms [33,34] such as deep neural networks (DNNs) [35,36], extreme gradient boosting (XGBoost) [37,38], and transfer learning (TL) [39–41], accelerating calculations and establishing reliable relationships between material compositions, structures, and properties that can be used to guide the design and discovery of new energy materials. Recently, some researches about ML to predict SE properties are reported. Chen et al. considered uniformity and ionic conductivity for evaluating SE films under the guidance of ML [42]. Wang et al. proposed a new solid polymer electrolyte design approach that integrated coarse-grained molecular dynamics (CGMD) with ML [43]. Zhao et al. introduced a framework of ML prediction for cubic Li-argyrodites, showing great potential in promoting rational design of advanced SEs. These researches provide new avenues and methods for the discovery of promising garnet-type SEs for SSBs [44].

Here, we pioneer the utilization of ML technologies to systematically accelerate the discovery of garnet-type SEs. Our work provides a comprehensive screening study integrating multiple critical factors such as σ_e, σ_i, and thermodynamic stability. We first collect 286 garnet structures with calculated band gaps (E_g) from the Materials Project (MP) database [45] and construct 29,008 garnets by combining four elements from 286 known garnets. Then, 7067 garnets are expected to be structurally stable through tolerance factor filtering. By feature construction and extraction based on element properties, we establish a classification model (XGB-*C*) and a regression model (XGB-*R*) on 286 garnets using XGBoost. The XGB-*C* model classifies the narrower band gap (NE_g, $E_g < 0.5$ eV) and the wider band gap (WE_g, $E_g > 0.5$ eV) with a high accuracy of 88.5%, and the XGB-*R* model predicts E_g for WE_g with a very low mean absolute error (MAE) of 0.25 eV, achieving a computed speed that is ~10^9 faster than ab initio calculations. Fleetingly, we employ the XGB-*C* model and XGB-*R* model to predict 7067 garnets and select 29 garnets with low σ_e ($< 3.6 \times 10^{-30}$ S cm^{-1}). Subsequently, we perform the reliable climbing image nudged elastic band (CI-NEB) method [46] to predict σ_i and use long-range ab initio molecular dynamics (AIMD) to evaluate the thermal dynamic stability at R_T and high temperature. Finally, we discovered 12 new garnets ($Dy_3Ga_2Li_3O_{12}$, $Dy_3Sc_2Li_3O_{12}$, $Gd_3Sc_2Li_3O_{12}$, $Ho_3Ga_2Li_3O_{12}$, $Ho_3Sc_2Li_3O_{12}$, $La_3Sc_2Li_3O_{12}$, $Nd_3Sc_2Li_3O_{12}$, $Pr_3Sc_2Li_3O_{12}$, $Sm_3Sc_2Li_3O_{12}$, $Tb_3Al_2Li_3O_{12}$, $Tm_3Ga_2Li_3O_{12}$, $Y_3Ga_2Li_3O_{12}$) with a high σ_i of 10^{-4}–10^{1} S cm^{-1} and good thermal stability at R_T and high temperature. These garnets will be great promising garnet-type SEs for solid-state LIBs. Our model successfully discovered 12 garnet-type SEs from 29,008 structures, significantly shortening the screening process of garnets by ~95 years computationally, saving a lot experimental costs, thus providing unique insight and means for the development of SEs for SSBs and promoting the development of advanced energy storage technologies.

2. Results and discussion

2.1. ML framework to discover garnet-type SEs

Our screening workflow for garnet-based electrolytes is described in Fig. 1. We first selected the proper site elements (Fig. S1 of the Supplementary Materials (SM)) for the A-, B-, C-, and X-sites based on the 286 known garnets in the Materials Project (MP) database [45], where tens of thousands of possible garnets (Fig. 1a) were generated. Then, we used the tolerance factor (T_f) [47] to preliminarily evaluate the structural stabilities of these garnets (Fig. 1b), leaving thousands of garnets that we considered potentially stable. Next, we performed feature engineering (feature construction, feature screening, and feature extraction) to determine the optimal features for the ML model (Fig. 1c). As shown in Fig. 1d, based on the 286 known garnets, we established a classification model (XGB-*C*) to classify the narrower band gap (NE_g, $E_g < 0.5$ eV) and the wider band gap (WE_g, $E_g > 0.5$ eV). Then, for the WE_g, we further established a regression model (XGB-*R*) to accurately predict E_g and quickly determine the large band gap (with low electronic conductivity) garnets for electrolytes. Therefore, for the potentially stable garnets in Fig. 1b, we used the well-trained XGB-*C* and XGB-*R* models to predict E_g in microseconds and obtain garnets with low electronic conductivity. Furthermore, small-scale first-principles calculations were performed to make accurate validations and determinations for the ultimate candidate garnet-based electrolytes, including global structural optimizations, electronic and ionic conductivity calculations, and thermal dynamical simulations (Fig. 1e). The detailed step-by-step screening process for garnet-type solid electrolytes is provided in Fig. S2.

2.2. Data generation

The garnet structure is known to consist of multitype polyhedrons, which are the dodecahedron {A}, the octahedron (B), and the tetrahedron [C]. The vertices of the dodecahedron, octahedron, and tetrahedron are occupied by anions $\langle X\rangle$. In this work, we collected 286 garnet structures with the same chemical form of $\{A\}_3(B)_2[C]_3\langle X\rangle_{12}$ and the space group of $Ia\bar{3}d$ from the MP database [45]. Among these structures, 79 garnets have been synthesized experimentally at ambient pressure and room temperature, while 207 garnets come from first-principles calculations. The statistics of site chemical elements are provided in Fig. S1. In Fig. 2a, the band gap distribution of these 286 garnets based on DFT calculations from MP database is presented [45], covering a wide range of 0–8 eV. Nearly 40% (107 garnets) of the band gaps are less than 0.5 eV (narrow E_g, NE_g for short), and the remaining 60% (179 garnets) are distributed relatively evenly. The statistical violin diagram

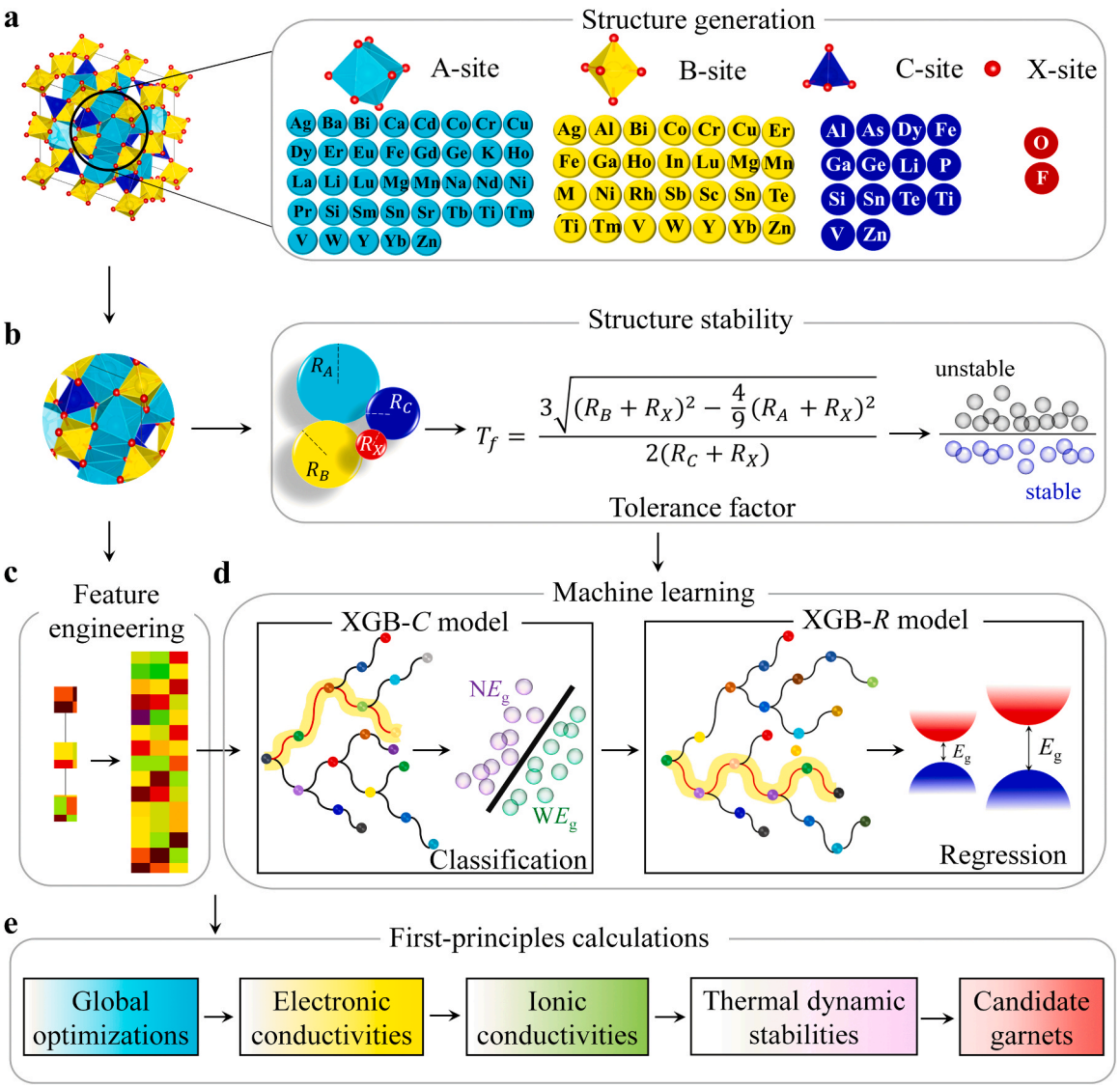

Fig. 1. Overview of the framework to discover garnet solid electrolytes. a Left panel, crystal structure of garnet materials with four element sites and space group of Ia$\bar{3}$d. Right panel, suitable element selection based on 286 known garnets for structure generation, where 37 elements are selected for the dodecahedron A-site, 28 elements for the octahedral B-site, 14 elements for the tetrahedron C-site, and two elements for the X-site. b Preliminary judgment of structural stability by tolerance factor, according to the ionic radius of four sites. c Feature engineering based on elemental properties for the ML model. d A narrower/wider band gap (NE_g/WE_g) classification model (XGB-*C*) and a band gap regression model (XGB-*R*) built for electronic conductivity prediction. e Further validation and screening for candidate garnets by first-principles calculations.

is shown in Fig. 2b. Clearly, 50% of E_g is in the range of 0–3 eV, while 90% is in the range of approximately 0–4 eV. The wide E_g coverage ensures that we can find the desired appropriate E_g in the unknown prediction dataset.

Furthermore, from the site elements of these 286 known garnets (see Fig. 1a and Fig. S1), we generated 29,008 different possible garnets as the initial dataset by the substitution of chemical species. Before using the ML model, we preliminarily judged the structural stability by a tolerance factor that depends on the ionic radius of the four sites (see Fig. 2c). Fig. 2d shows the distribution of T_f for 29,008 structures, and since the structure is considered stable when its T_f meets $0.9 < T_f < 1.1$ (see Methods), 7067 structures are selected from 29,008 structures for further prediction.

2.3. ML model for garnet materials

To obtain large band gap garnets quickly from 7067 structures at the lowest cost, it is efficient to establish reliable ML models for predicting the band gaps rather than using many experimental measurements or DFT calculations. According to Fig. 2a and b, a considerable portion of E_g (107 garnets, account for ~40%) is concentrated at 0–0.5 eV, resulting in an imbalanced dataset, which further destabilizes the ML models and affects the final prediction accuracy. To remove this barrier, we established a classification model to classify the narrower band gap (NE_g, $E_g < 0.5$ eV) and the wider band gap (WE_g, $E_g > 0.5$ eV). Then, for the WE_g (179 garnets), we further established a regression model (XGB-*R*) for accurately predicting E_g to quickly determine the large band gap (low electronic conductivity, see Methods) garnets for electrolytes.

A precondition is the determination of features that are the inputs for ML. Based on the relationship between accessible element properties and material properties [38,48], we preliminarily constructed the feature set of seven elemental properties: dipole polarizability (*P*), atomic number (AN), covalent radius (*cr*), van der Waals radius (*vr*), EN_Ghosh (EG), first ionization energy (IE), and valence electron (VE) (see full list of features in Table S1 of SM). For four site elements, a 28-dimensional feature vector was constructed for each structure. Then,

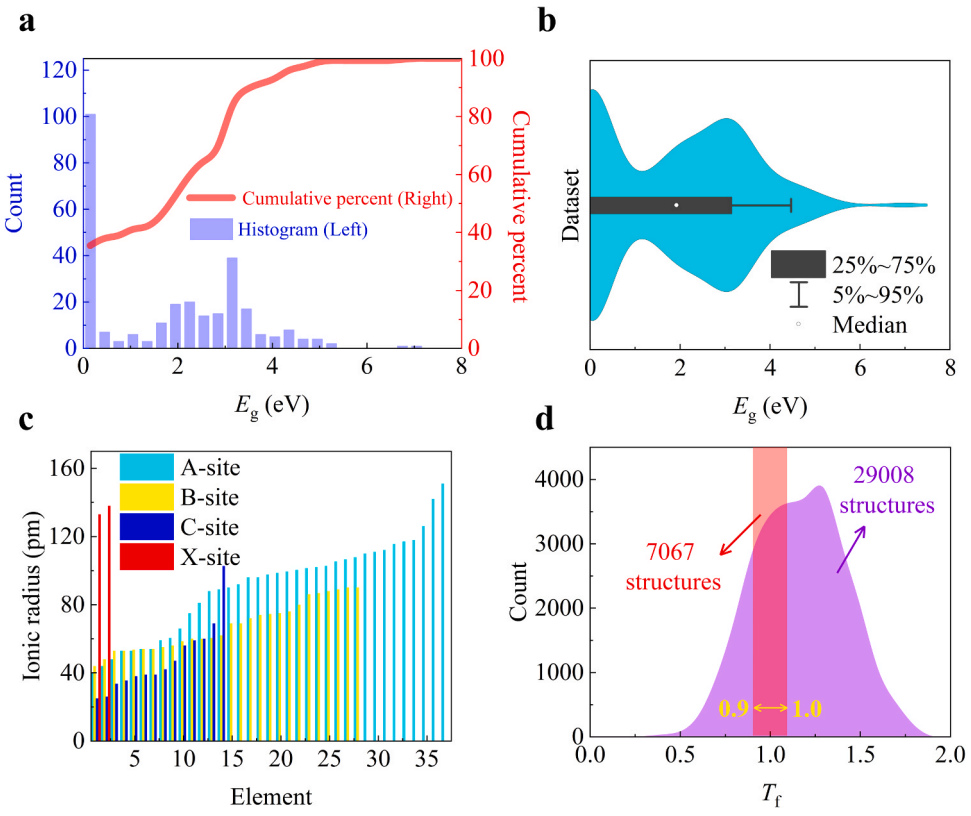

Fig. 2. Garnet dataset statistics. a Band gap histogram (left) together with cumulative percent (right) for 286 known garnets. b Statistical violin diagram of E_g for 286 known garnets. c Ionic radius for four site elements. d Distribution of T_f for 29,008 structures, and 7067 structures with $0.9 < T_f < 1.1$ are considered stable.

feature screening was implicitly accomplished by XGBoost, and feature importance was evaluated by the F-score, which can measure the ability of the algorithm to distinguish two categories of features and is one of the best criteria for ranking the importance of features. As shown in Fig. 3a, we extracted 16 relatively important features with F-scores greater than 50 (the full ordering of features is provided in Fig. S3 of SM), which are the first ionization of the B-site (IE_B), atomic number of the A-site (AN_A), and dipole polarizability of the A-site (P_A). The heat map of Pearson correlation coefficients (PCCs) from − 1.0 to 1.0 for these 16 features is shown in Fig. 3b, and most PCCs are between − 0.2 and 0.2 and show weak linear relationships, which indicates the non-redundancy of features. The XGB-*C* model is constructed based on these 16 features to classify NE_g/WE_g, and 10-fold cross-validations (CVs) were performed to evaluate the model accuracy. We obtained the optimal model through the grid search method for hyper-parameters (see Table S2). As shown in Fig. 3c, the receiver operating characteristic (ROC) curves between the true positive rate and false positive rate of 10-fold CVs on the testing set are presented, together with the corresponding AUCs (an area under the ROC curves). The testing AUCs are 0.828, 0.966, 0.793, 0.897, 0.897, 0.897, 0.893, 0.893, 0.893, and 0.893, respectively, and 0.885 for average (see training and testing results in Table S3), signifying the excellent discrimination between the NE_g and WE_g by the XGB-*C* model and the sensitivities and effectiveness of 16 features for NE_g/WE_g. More discussion of feature engineering is provided in Note S1. In Fig. 3d, the band gaps of the remaining 7067 potentially stable garnets are predicted by the well-trained XGB-*C* model, where 3266 garnets have NE_g and 3801 garnets have WE_g.

Furthermore, for the WE_g, we established a regression model (XGB-*R*) to subtly predict E_g, and in this way, we could quickly select garnets with larger band gaps, namely, low electronic conductivities. Similarly, we constructed the initial set of features using the above seven elemental properties and determined 15 relatively important features with F-scores > 100 through feature screening and extraction by XGBoost (Fig. 4a; see the full ordering of features in Fig. S4). The heat map of PCCs for these 15 features in Fig. 4b also shows weak linear relationships, which ensures the robust training of the XGB-*R* model. We used two metrics to measure the accuracy of the XGB-*R* model: the mean absolute errors (MAEs, eV) and coefficient of determination (R^2). The testing results with MAEs of 10-fold CVs for the XGB-*R* model are shown in Fig. 4c. The ML predicted band gaps have a high consistency with the band gaps calculated by the Perdew-Burke-Ernzerhof (PBE) functional. The MAEs are 0.19, 0.28, 0.33, 0.36, 0.12, 0.30, 0.13, 0.21, 0.37, and 0.16, respectively, and 0.25 for average. The details of R^2 are provided in Table S3 of SM, which has an average of 0.866. More plots of 10-fold cross validations are shown in Fig. S5. The above results demonstrate the outstanding performance of the XGB-*R* model, and more discussion of feature engineering and model rational analysis are provided in Notes S1 and S2. Then, the well-trained model was applied to the 3801 garnets with WE_g to predict their band gaps, and the prediction results are shown in Fig. 4d. We notice that the predicted band gaps basically present a normal distribution (blue histogram) between 0.5 and 7.0 eV, and the cumulative percent curve (red curve) almost presents an S-shape. The short dashed line in Fig. 4d denotes the E_g of 4.0 eV, which is considered the E_g of insulators that have extremely low electronic conductivities ($\sigma_e < 3.6 \times 10^{-30}$ S cm^{-1}). Finally, we counted 210 new garnets with $E_g > 4.0$ eV (outside of the known 286 structures), where 161 garnets with $X = F^-$ and 49 with $X = O^{2-}$ (see full list in Tables S4 and S5 of SM) deserve to be studied further for solid electrolytes.

Since our objective is to screen and discover garnets with low electronic conductivities and high ionic conductivities, we narrowed the study range down to 210 garnets with $E_g > 4.0$ eV ($\sigma_e < 3.6 \times 10^{-30}$ S cm^{-1}) (see Fig. S2). In addition, considering that oxide-type electrolytes generally exhibit high ionic conductivities and high mechanical strength and that halides are more difficult to prepare experimentally than oxides [49–51], we further studied 49 oxides ($X = O^{2-}$) in further first-principles calculations (see the list in Table S4). During the

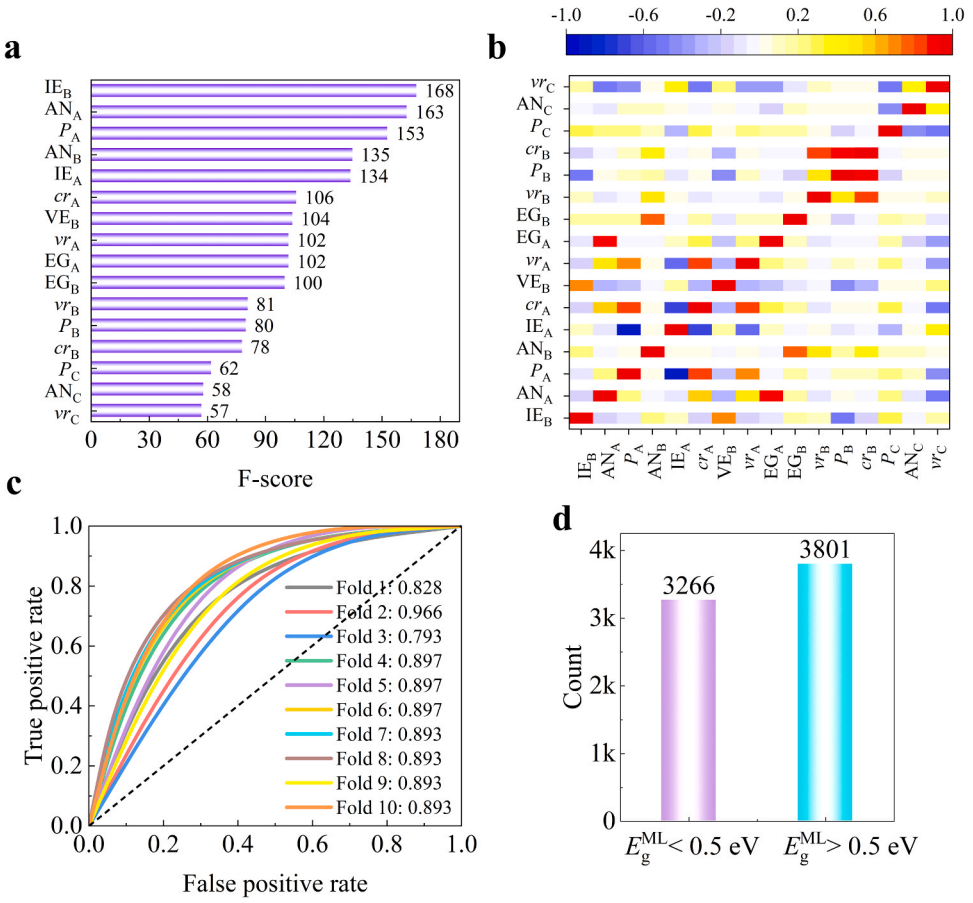

Fig. 3. Results of XGB-*C* model. a 16 relatively important features with F-scores > 50 that were screened and extracted by XGBoost. b Heat map of Pearson correlation coefficients (PCCs) from − 1.0 (blue) to 1.0 (red) for these 16 features. c Receiver operating characteristic (ROC) curves obtained from 10-fold cross-validations, together with the AUCs. d Classification of 7067 potentially stable garnets by the XGB-*C* model, where 3266 garnets have predicted band gaps (E_g^{ML})< 0.5 eV and 3801 have E_g^{ML} > 0.5 eV.

structural optimizations, we found that two structures ($Dy_3Ga_2Al_3O_{12}$ and $Na_3Sc_2Li_3O_{12}$) change significantly, resulting in the final non-convergence, which may be caused by the mismatches between the elements (since their stabilities are roughly evaluated by T_f), and we excluded them. The E_g (predicted and calculated) of the other 47 structures are shown in Fig. 5a and Table S4, and there is a small difference between the E_g predicted by the XGB-*R* model and those calculated by DFT for most structures. Only a few structures such as $Co_3Al_2Li_3O_{12}$, $V_3Al_2Li_3O_{12}$, and $Y_3Al_2Si_3O_{12}$, whose E_g are less than 0.5 eV or quite different from the DFT calculations, are also within the allowable error range of the XGB-*C* and XGB-*R* models. The above results once again prove the accuracy of our models, which can be used to accurately classify and predict the electronic conductivities of garnet structures.

Moreover, we usually spent extensive time on the DFT calculations for garnet structures, as shown in Fig. 5b and Table S6, each structure taking approximately 101,597 s on average (approximately 1.2 days), whereas the prediction time of both XGB-*C* and XGB-*R* models for 7067 garnet structures can be almost negligible (each one in milliseconds), manifesting a computed speed that is faster than using DFT calculations on supercomputers by a factor of $\sim 10^9$, the calculation time of first-principles for totally 29,008 garnet structures, which is approximately 95 years, is greatly shortened, thus saving significant costs and time for finding new garnets. In particular, in experiments, obtaining a solid electrolyte and its properties generally requires steps such as synthesis and testing. After our preliminary calculation, it takes at least 64 h to synthesize and test a single SE [52]. In this way, the experimental cycle will be tremendously shortened for a total of 29,008 garnet structures using our AI method. In addition, a key factor affecting the application of power batteries is their high production cost. At present, the materials of solid-state batteries are controlled mainly by the oxide solid electrolyte LLZO, whose price is approximately \$2000 kg^{-1}. After an estimate, our screening method can save at least \$57 million for the experimental cost [53].

2.4. Electronic properties of 29 garnets

In batteries, electronic conduction across the electrolytes must be negligible. In particular, recent studies have revealed that lithium dendrites are more likely to form in solid electrolytes because of the high electronic conductivity of solid electrolytes [25]. Therefore, from 47 garnets in Table S4, we strictly selected 29 garnets with calculated E_g larger than 4.0 eV for detailed study to ensure extremely low electronic conductivities. The lattice lengths, lattice angles, predicted E_g and calculated E_g are shown in Table 1. Some garnets, the predicted E_g of which is larger than 4.0 eV, are also excluded from further study if the calculated E_g is slightly less than 4.0 eV. (such as $Er_3Ga_2Al_3O_{12}$, the predicted E_g and calculated E_g are 4.04 eV and 3.98 eV, respectively). In these 29 structures, the lattice lengths and angles do not change significantly during the global geometric optimizations, which indicates the stability of the geometric structures. The density of states (DOSs) of the 29 garnets are shown in Fig. 6 and Figs. S6 and S7, where the conduction band minima (CBM) are away from the Fermi level (energy = 0 eV) and dominated by the A-site (red areas) and B-site (green areas) atoms, while the valence band maxima (VBM) are close to the Fermi level and contributed by the X-site (cyan areas) atoms for the most part, indicating that the elements in garnet structures have an important influence on their electronic conductivity, which is also one of the research drivers of this work.

Wide band gaps allow all these structures to have electronic conductivity below 3.6×10^{-30} S cm^{-1}, which satisfies one of the conditions for solid electrolytes. In addition, each of these structures can be a

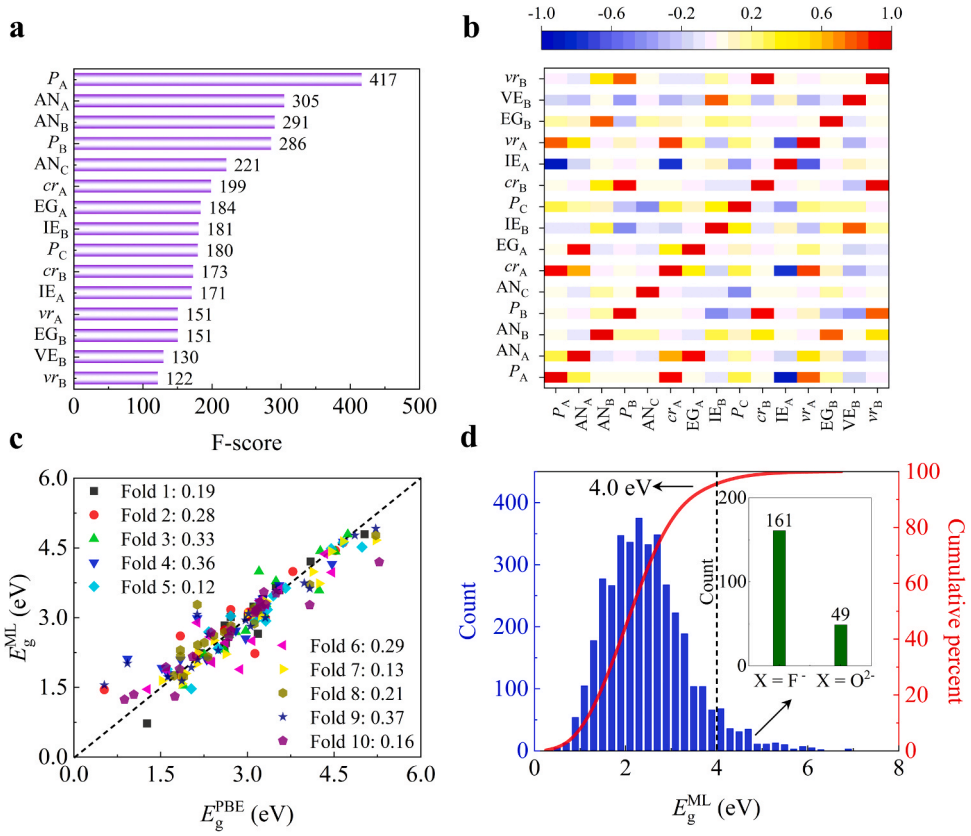

Fig. 4. Results of XGB-*R* model. a 15 relatively important features with F-scores > 100 that were screened and extracted by XGBoost. b Heat map of PCCs from − 1.0 (blue) to 1.0 (red) for these 15 features. c Correlation plots of E_g against PBE and ML on 10-fold CVs. d Regression prediction for 3801 wider band gap garnets by the XGB-*R* model, where 210 new garnets were selected that have $E_g^{ML} > 4.0$ eV and consist of 161 halides ($X = F^-$) and 49 oxides ($X = O^{2-}$).

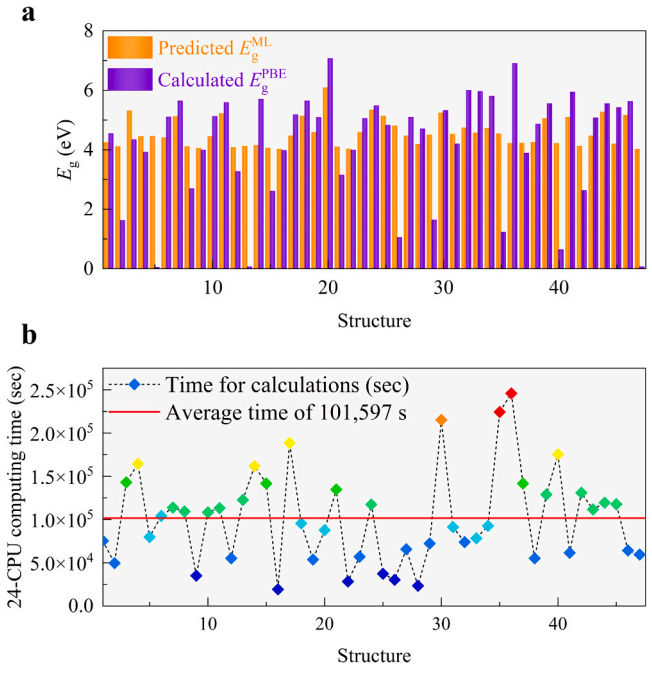

Fig. 5. DFT calculations for 47 garnet structures. a Comparison of E_g (E_g^{ML}) predicted by the XGB-*R* model and E_g (E_g^{PBE}) calculated by DFT for 47 garnet structures. The complete values of E_g are provided in Table S4 of SM. b Calculation time (sec) for 47 garnet structures on 24-CPU supercomputers. The red line denotes the average time of 101,597 s (approximately 1.2 days).

candidate for the corresponding solid electrolyte; for example, $Ca_3Ga_2Al_3O_{12}$ may be applied to solid-state AIBs, $Ca_3Sc_2Li_3O_{12}$, $Dy_3Ga_2Li_3O_{12}$, and $Er_3Ga_2Li_3O_{12}$ for solid-state LIBs, and $Na_3Ga_2Si_3O_{12}$ for SIBs. Since solid electrolyte suitability is the primary motivation for examining these properties of electrons and ions, more calculations and analysis of the ionic properties of these 29 garnet structures are necessary.

2.5. *Ionic conductivities of 29 garnets*

In addition to extremely low electronic conductivity, high ionic conductivity at R_T is also one of the most critical and important conditions for a good solid electrolyte. We estimated the diffusion coefficient by simulating the diffusion of ions within the crystal by the reliable climbing image nudged elastic band (CI-NEB) method [46], which has been widely used in simulating the diffusion of ions and its high computational precision can guide the experiments [54–57]. Then, we obtained the reaction path and the migration energy barrier (or "activation energy", E_a), as well as the final ionic conductivity σ_i. The full information is presented in Table 2 and Table S7. We found that $Tm_3Sc_2Li_3O_{12}$ has a maximum E_a of 2.06 eV and a minimum σ_i of 9.70×10^{-33} S cm^{-1}, while $Dy_3Ga_2Li_3O_{12}$ has a minimum E_a of 0.12 eV and a maximum σ_i of 3.24 S cm^{-1}. In general, "superionic conductors" are materials with ionic conductivities of 1.0×10^{-6} S cm^{-1} comparable to the ionic conductivity of liquid electrolytes, and low ion migration activation energies of less than 0.4 eV at room temperature. Following this standard, we selected 12 Li-ion "superionic conductors" from Table S7: $Dy_3Ga_2Li_3O_{12}$, $Dy_3Sc_2Li_3O_{12}$, $Gd_3Sc_2Li_3O_{12}$, $Ho_3Ga_2Li_3O_{12}$, $Ho_3Sc_2Li_3O_{12}$, $La_3Sc_2Li_3O_{12}$, $Nd_3Sc_2Li_3O_{12}$, $Pr_3Sc_2Li_3O_{12}$, $Sm_3Sc_2Li_3O_{12}$, $Tb_3Al_2Li_3O_{12}$, $Tm_3Ga_2Li_3O_{12}$, and $Y_3Ga_2Li_3O_{12}$ (Table 2). Visualizations of the migration path and energy shift are provided in Figs. S8–S13 of

Table 1
Lattice lengths, lattice angles, predicted E_g and calculated E_g for 29 garnets, where the predicted E_g and calculated E_g are both larger than 4.0 eV.

Formula	Lattice length (Å)			Lattice angle (°)			E_g^{ML} (eV)	E_g^{PBE} (eV)
	a	*b*	*c*	*α*	*β*	*γ*		
$Ca_3Ga_2Al_3O_{12}$	10.78	10.74	10.79	109.38	109.52	109.41	4.23	4.54
$Ca_3Sc_2Li_3O_{12}$	11.34	10.22	11.22	107.66	111.62	107.52	5.30	4.33
$Dy_3Ga_2Li_3O_{12}$	11.00	10.88	10.93	109.25	109.72	109.47	4.40	5.10
$Dy_3Sc_2Li_3O_{12}$	11.11	11.09	11.09	109.58	109.68	109.17	5.12	5.64
$Er_3Ga_2Li_3O_{12}$	10.87	10.87	10.86	109.47	109.47	109.49	4.44	5.12
$Er_3Sc_2Li_3O_{12}$	11.02	11.02	11.02	109.57	109.57	109.28	5.21	5.58
$Gd_3Sc_2Li_3O_{12}$	11.06	11.01	11.02	109.51	109.71	109.25	4.14	5.70
$Ho_3Ga_2Li_3O_{12}$	10.93	10.84	10.90	109.31	109.64	109.42	4.46	5.17
$Ho_3Sc_2Li_3O_{12}$	11.06	11.05	10.05	109.56	109.62	109.26	5.13	5.64
$La_3Sc_2Li_3O_{12}$	11.36	11.37	11.36	109.46	109.46	109.50	4.58	5.08
$Li_3Al_2Li_3O_{12}$	10.38	10.18	10.20	109.07	109.89	109.77	6.08	7.07
$Lu_3Ga_2Li_3O_{12}$	10.74	10.80	10.75	109.58	109.36	109.53	4.58	5.05
$Lu_3Sc_2Li_3O_{12}$	10.93	10.92	10.92	109.58	109.59	109.27	5.33	5.48
$Mg_3Al_2Al_3O_{12}$	10.11	10.11	10.44	109.02	109.04	109.06	5.13	4.82
$Mg_3Ga_2Li_3O_{12}$	10.30	10.26	10.30	109.38	109.52	109.42	4.46	5.09
$Na_3Ga_2Si_3O_{12}$	10.51	10.51	10.51	109.47	109.47	109.47	4.18	4.70
$Na_3Sc_2Al_3O_{12}$	10.08	11.04	11.18	109.46	109.61	108.90	5.23	5.32
$Na_3Sc_2P_3O_{12}$	10.63	10.63	10.63	109.46	109.47	109.48	4.52	4.19
$Nd_3Sc_2Li_3O_{12}$	11.33	11.26	11.30	109.30	109.55	109.53	4.73	5.99
$Pr_3Sc_2Li_3O_{12}$	11.39	11.26	11.36	109.26	109.72	109.30	4.56	5.96
$Sm_3Sc_2Li_3O_{12}$	11.28	11.13	11.19	109.29	109.83	109.35	4.72	5.80
$Sr_3Er_2Li_3O_{12}$	10.78	10.74	10.79	109.38	109.52	109.41	4.21	6.90
$Sr_3Sc_2Al_3O_{12}$	11.21	11.20	11.20	109.46	109.49	109.46	4.24	4.86
$Sr_3Sc_2Li_3O_{12}$	10.93	10.71	11.58	110.59	111.33	103.56	5.04	5.55
$Tb_3Al_2Li_3O_{12}$	10.85	10.87	10.86	109.55	109.50	109.36	5.09	5.94
$Tm_3Ga_2Li_3O_{12}$	10.84	10.87	10.84	109.52	109.40	109.54	4.46	5.07
$Tm_3Sc_2Li_3O_{12}$	11.00	11.00	11.01	109.55	109.56	109.30	5.27	5.55
$Y_3Ga_2Li_3O_{12}$	10.82	10.79	10.80	109.44	109.53	109.48	4.19	5.42
$Y_3Sc_2Li_3O_{12}$	10.95	10.93	10.95	109.57	109.64	109.20	5.16	5.62

SM.

As shown in Fig. 7, 12 garnets (squares, above the dotted line of 10^{-4} S cm^{-1}) show high ionic conductivities ($\sigma_i > 1.0 \times 10^{-4}$ S cm^{-1}) and can even compete with the best superionic conductor materials experimentally available today. For instance, $Li_{10.35}Si_{1.35}P_{1.65}S_{12}$, $Li_7P_3S_{11}$, and LLZO (garnet-type) show $\sim 6.5 \times 10^{-3}$ S cm^{-1}, $\sim 4.1 \times 10^{-3}$ S cm^{-1}, and 10^{-4}–10^{-3} S cm^{-1}, respectively [58–61], and they have been used for SSBs in the laboratory owing to their high σ_i. However, their σ_i values are slightly inferior to our predicted structures of $Y_3Ga_2Li_3O_{12}$ (0.24 S cm^{-1}) and $Pr_3Sc_2Li_3O_{12}$ (0.12 S cm^{-1}) and much worse than our predicted candidates of $Dy_3Ga_2Li_3O_{12}$ (3.24 S cm^{-1}) and $Ho_3Ga_2Li_3O_{12}$ (1.52 S cm^{-1}). Additionally, the 12 predicted new materials are pure garnets, whose ionic conductivities have exceeded the ionic conductivity of many superionic conductors obtained through doping and complex experimental designs. Perhaps through doping and other means, the ionic conductivities of the 12 predicted new structures will be further improved. These 12 structures show high ionic conductivities that can directly improve the mobility of lithium ions, weaken the concentration polarization during charge and discharge, and improve the power density of the SSBs. Additionally, they greatly expand the family of SEs and bring a new dawn for superionic SEs.

Although there are some rare metal elements (i.e. Sc) in the screened 12 garnets, their excellent properties still have broad applications. In addition, some garnet structures with low electronic conductivities were screened out, as shown in Table S7 of SM. Although their simulated ionic conductivities are not high, they can be improved experimentally (doping or composite technology) to become candidate SEs for SSBs. Such as $Ca_3Sc_2Li_3O_{12}$ (3.50×10^{-6} S cm^{-1}), $Er_3Ga_2Li_3O_{12}$ (1.33×10^{-8} S cm^{-1}), and $Li_3Al_2Li_3O_{12}$ (1.75×10^{-12} S cm^{-1}) in Table S7. Moreover, we also calculated the migrations of Al ions within $Ca_3Ga_2Al_3O_{12}$ (8.21×10^{-9} S cm^{-1}) and $Mg_3Al_2Al_3O_{12}$ (1.28×10^{-9} S cm^{-1}) and Na ions within $Na_3Ga_2Si_3O_{12}$ (6.68×10^{-12} S cm^{-1}) and $Na_3Sc_2P_3O_{12}$ (2.12×10^{-17} S cm^{-1}), providing a basis for research into solid-state AIBs and SIBs even though they show low ionic conductivity.

2.6. Thermal dynamic stabilities of 12 garnets by AIMD

We successfully discovered 12 promising garnet-type Li-ion SEs with $\sigma_e < 3.6 \times 10^{-30}$ S cm^{-1} and $\sigma_i > 10^{-4}$ S cm^{-1} through ML. However, the stabilities of these structures are preliminarily determined by T_f, which is obviously rough and insufficient. As a key factor of SEs, thermal stability needs to be further studied [22,30]. Therefore, we further used ab initio molecular dynamics (AIMD) to analyze and evaluate the thermal stabilities of these 12 garnets (300 K and 1000 K). As shown in Fig. 8 and Figs. S14 and S15, during the dynamic process of up to 5 ps, the total energy fluctuations of these systems are rapidly stabilized and fluctuate within a narrow range of approximately 3.0 eV. Meanwhile, we extracted snapshots for these structures every 1 ps, and there were no obvious changes in the cell structures. These results indicate that the 12 predicted garnet structures are stable at R_T and high temperature and promising for use as solid electrolyte materials for SSBs in practical applications.

3. Conclusions

In summary, we present an effective target-driven machine learning approach to discover garnet-type solid electrolytes for SSBs. During this process, we established a classification model of XGB-*C* with a high accuracy of 88.5% and a regression model XGB-*R* with a low MAE of 0.25 eV to predict the electronic conductivity of garnet materials. These two models provide a computed speed that is faster than using DFT calculations on supercomputers by a factor of $\sim 10^9$, helping us to quickly select garnets with low electronic conductivities. We then successfully identified 12 promising SEs ($Dy_3Ga_2Li_3O_{12}$, $Dy_3Sc_2Li_3O_{12}$, $Gd_3Sc_2Li_3O_{12}$, $Ho_3Ga_2Li_3O_{12}$, $Ho_3Sc_2Li_3O_{12}$, $La_3Sc_2Li_3O_{12}$, $Nd_3Sc_2Li_3O_{12}$, $Pr_3Sc_2Li_3O_{12}$, $Sm_3Sc_2Li_3O_{12}$, $Tb_3Al_2Li_3O_{12}$, $Tm_3Ga_2Li_3O_{12}$, $Y_3Ga_2Li_3O_{12}$) with $\sigma_e < 3.6 \times 10^{-30}$ S cm^{-1} and $\sigma_i > 10^{-4}$ S cm^{-1} from 29,008 garnet structures. The proposed method directly spans 95-year computational cycle for screening garnet electrolytes, not to mention the experimental cycle, thereby saving approximately at

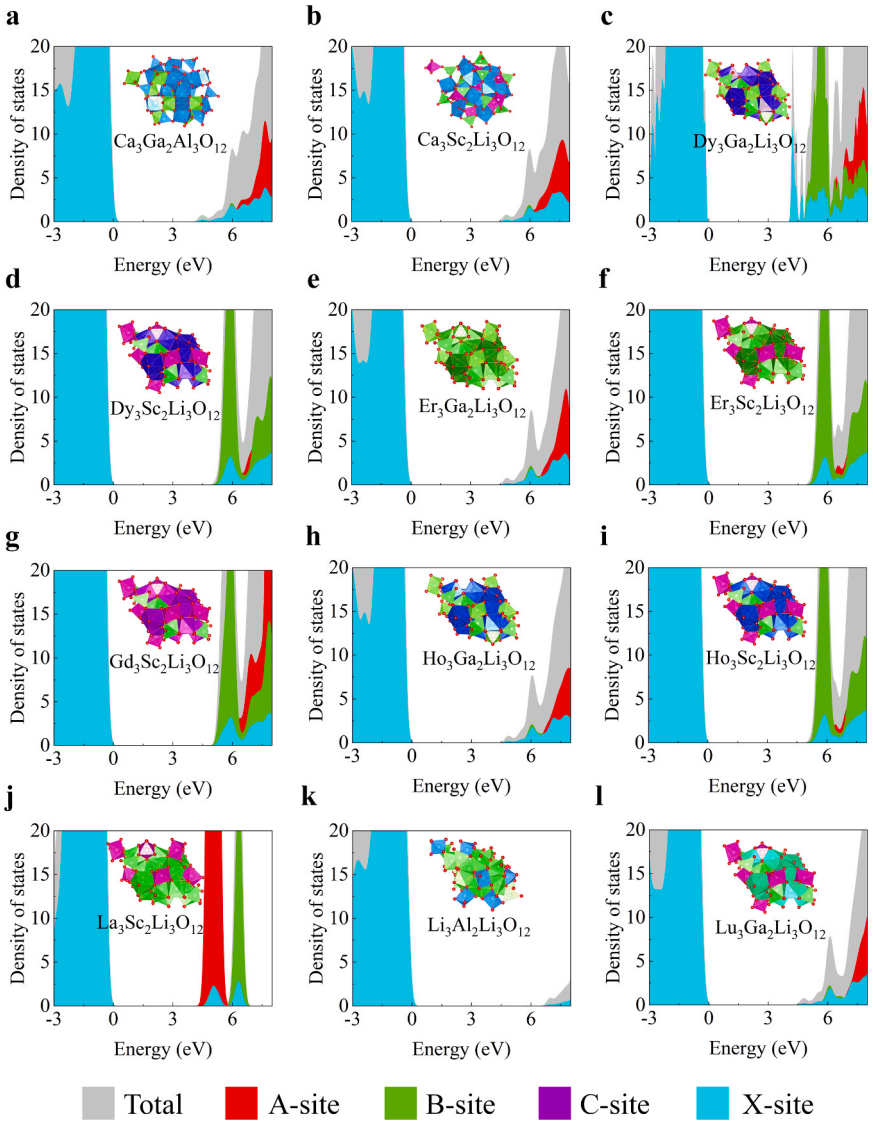

Fig. 6. Density of states (DOSs) for 12 garnet structures with $E_g > 4.0$ eV. a $Ca_3Ga_2Al_3O_{12}$. b $Ca_3Sc_2Li_3O_{12}$. c $Dy_3Ga_2Li_3O_{12}$. d $Dy_3Sc_2Li_3O_{12}$. e $Er_3Ga_2Li_3O_{12}$. f $Er_3Sc_2Li_3O_{12}$. g $Gd_3Sc_2Li_3O_{12}$. h $Ho_3Ga_2Li_3O_{12}$. i $Ho_3Sc_2Li_3O_{12}$. j $La_3Sc_2Li_3O_{12}$. k $Li_3Al_2Li_3O_{12}$. l $Lu_3Ga_2Li_3O_{12}$. The optimized structures are also presented in each DOS.

Table 2
Diffusion coefficients, migration energy barriers, and ionic conductivities at room temperature for 12 garnets with calculated E_g values larger than 4.0 eV and energy barriers less than 0.4 eV.

Formula	Diffusion coefficient ($cm^2\ s^{-1}$)	Energy barrier (eV)	Ionic conductivity (S cm^{-1})
$Dy_3Ga_2Li_3O_{12}$	6.58×10^{-5}	0.12	3.24×10^{0}
$Dy_3Sc_2Li_3O_{12}$	2.33×10^{-8}	0.33	1.10×10^{-3}
$Gd_3Sc_2Li_3O_{12}$	6.59×10^{-8}	0.30	3.17×10^{-3}
$Ho_3Ga_2Li_3O_{12}$	3.05×10^{-5}	0.14	1.52×10^{0}
$Ho_3Sc_2Li_3O_{12}$	2.14×10^{-6}	0.21	1.02×10^{-1}
$La_3Sc_2Li_3O_{12}$	6.17×10^{-8}	0.30	2.71×10^{-3}
$Nd_3Sc_2Li_3O_{12}$	1.89×10^{-6}	0.22	8.43×10^{-2}
$Pr_3Sc_2Li_3O_{12}$	2.72×10^{-6}	0.21	1.20×10^{-1}
$Sm_3Sc_2Li_3O_{12}$	3.96×10^{-7}	0.26	1.81×10^{-2}
$Tb_3Al_2Li_3O_{12}$	9.06×10^{-9}	0.35	4.55×10^{-4}
$Tm_3Ga_2Li_3O_{12}$	1.04×10^{-8}	0.35	5.26×10^{-4}
$Y_3Ga_2Li_3O_{12}$	4.69×10^{-6}	0.19	2.40×10^{-1}

least $57 million in experimental costs. These new garnet-type SEs are expected to perform in solid-state LIBs, AIBs, and SIBs, thus improving the safety, performance, and lifetime of our state-of-the-art energy storage technology.

The discovery of unknown garnet materials satisfying the many-property conditions for SEs is heart-stirring, and only 12 of the 29,008 garnets are selected, suggesting that it is naturally and inherently difficult to discover and design SE materials with excellent performance. During our screening process, garnets with extremely low σ_e of 3.6×10^{-30} S cm^{-1} were selected. Garnets with σ_e higher than 3.6×10^{-30} S cm^{-1} could be further improved as a candidate electrolyte material, but it does not rule out that other predicted materials could achieve better performances through doping and structural design. Furthermore, we have been working on the development of high-precision ionic conductivity models, but the limited available data make it difficult to make more accurate predictions. We hope that as more data become available, the model described here may be further refined, achieving a shortcut for fully automated screening of solid electrolyte materials.

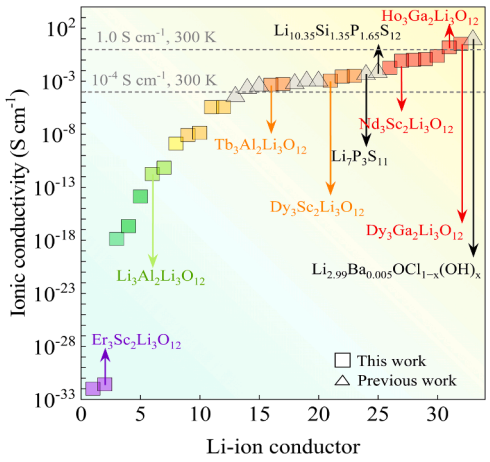

Fig. 7. Visualization and comparison of ionic conductivity for 29 garnet structures and previous ionic conductors. The squares represent the new garnet we discovered, the color represents the value of σ_i, increasing from purple to red, and the triangles represent the ionic conductors from previous studies. The dotted lines denote σ_i of 1.0 S cm^{-1} and 10^{-4} S cm^{-1} at R_T (300 K).

4. Methods

4.1. Tolerance factor for garnets

With the basic geometrical relationship established, the tolerance factor (T_f) of garnet structures can be constructed by the ionic radius of all the chemical species constituting garnet [47]. The proposed T_f as below:

$$T_f = \frac{3\sqrt{(R_B + R_X)^2 \quad - \quad \frac{4}{9}(R_A + R_X)^2}}{2(R_C + R_X)} \tag{1}$$

The T_f of over 100 different garnet structures has been calculated in the range of 0.75–1.33, similar to the T_f of perovskite structures. For real garnet-based compounds, the ideal T_f is expected to fluctuate by approximately 1; therefore, in this work, we select likely stable garnets with T_f in the range of 0.9–1.1.

4.2. Machine learning model

The machine learning model in this work is implemented by the classification model (XGB-*C*) and regression model (XGB-*R*), which are all based on the extreme gradient boosting (XGBoost) algorithm [62]. Overall, the model between the predicted value Y_i^{pred} and input X_i can be mathematically written as:

$$Y_i^{pred} = \sum_k f_k(X_i) \tag{2}$$

where k is the number of decision trees, and f is a function in the functional space. The loss function that contains the gradient boosting algorithm loss and regularization term in the training process is defined as:

$$L(\varnothing) = \sum_{i=1}^{n} l\left(Y_i^{pred} - Y_i^{real}\right) + \sum_k \left(\psi\rho + \frac{1}{2}\lambda\|\omega\|\right) \tag{3}$$

where ρ is the number of leaf nodes in the decision tree, and ω is the score of leaf nodes. ψ and λ are the default coefficients of the regularization term to limit the number of leaf nodes and smooth the score of leaf nodes.

To obtain the optimal model, the determination of hyper-parameters is essential. In both the XGB-*C* and XGB-*R* models, the hyper-parameters (the maximum number of trees, the step size of each iteration, the percentage of samples that are randomly sampled per tree, the percentage of features sampled at random per tree, and the maximum depth of the tree) are selected by the grid search method. More details are provided in Table S2 of SM. In addition, ten-fold cross-validation (CV) is applied to evaluate the accuracy of the two models, where the data are split equally into ten nonoverlapping folds, nine folds are used as the training set and the remaining fold works as validation.

4.3. First-principles calculations

The Vienna *Ab initio* Simulation Package (VASP) is employed for first-principles calculations [63]. The projected augmented wave (PAW) method [64,65] is applied to describe ion-electron interactions along with the Perdew-Burke-Ernzerhof (PBE) exchange-correlation function under generalized gradient approximation (GGA) [66], where the Coulomb U and exchange J parameters are considered ($U_{\text{eff}} = U - J$). The cutoff energy of 500 eV is set for the plane-wave basis, and the structure optimization process is stopped until an energy convergence lower than 10^{-5} eV and atomic force less than 0.03 eV/Å. The initial garnet structure is constructed in a supercell of a 2 × 2 × 2 unit cell with a total of 80 atoms. Brillouin zone integration is performed using a 2 × 2 × 2 k-point mesh for the cubic phase.

Ab initio molecular dynamics (AIMD) is applied to evaluate the thermal stabilities of garnets in a supercell of 2 × 2 × 2 unit cells. A total of 5000 fs of kinetic process was carried out for each garnet with a time step of 2 fs. The temperature is controlled at 300 K and 1000 K in the whole process based on the Nosé -Hoover thermostat [67,68].

4.4. Electronic conductivity calculations

Electronic conduction across the electrolyte must be minimal. In this work, we screened wider band gap ($E_g > 4.0$ eV) to ensure low electronic conductivity σ_e. σ_e can be calculated by E_g approximated by follows [69]:

$$\sigma_e = (m_e + m_h)q\sqrt{D_c D_V}e^{-\frac{E_g}{2kT}} \tag{4}$$

where m_e and m_h denote the electronic and hole mobilities, D_c and D_V are the DOSs in the conduction and valence bands, k is the Boltzmann constant, and T is the temperature. We used standard parameters for crystalline silicon: $m_e = 1430$ cm^2 V^{-1} s^{-1}, $m_h = 480$ cm^2 V^{-1} s^{-1}, $D_c = 2.89 \times 10^{19}$ cm^{-1}, and $D_V = 3.13 \times 10^{19}$ cm^{-1}. These parameters give $\sigma_e = 3.6 \times 10^{-30}$ S cm^{-1} if $E_g = 4.0$ eV at R_T.

4.5. Ionic conductivity calculations

Ionic conduction across the electrolyte must be maximal. To calculate the ionic conductivity, we searched for possible ion migration pathways using the climbing image nudged elastic band (CI-NEB) method [46]. For each system, four initial images between two local optimized structures are first constructed by linear interpolation and then fully relaxed. The diffusion coefficient (D) is estimated from transition state theory [70] as:

$$D = \frac{1}{2}va^2e^{-\frac{E_a}{kT}} \tag{5}$$

where v is the lattice vibrational frequency with a typical value of 10^{13} Hz, a is the hop distance, E_a is the migration energy barrier, k is the Boltzmann constant, and T denotes the temperature. From the diffusivity, the ionic conductivity σ_i is estimated by the Nernst-Einstein equation [70]:

$$\sigma_i = \frac{Nq^2}{VkT}D \tag{6}$$

where V is the volume of the system and q is the charge of the mobile-ion

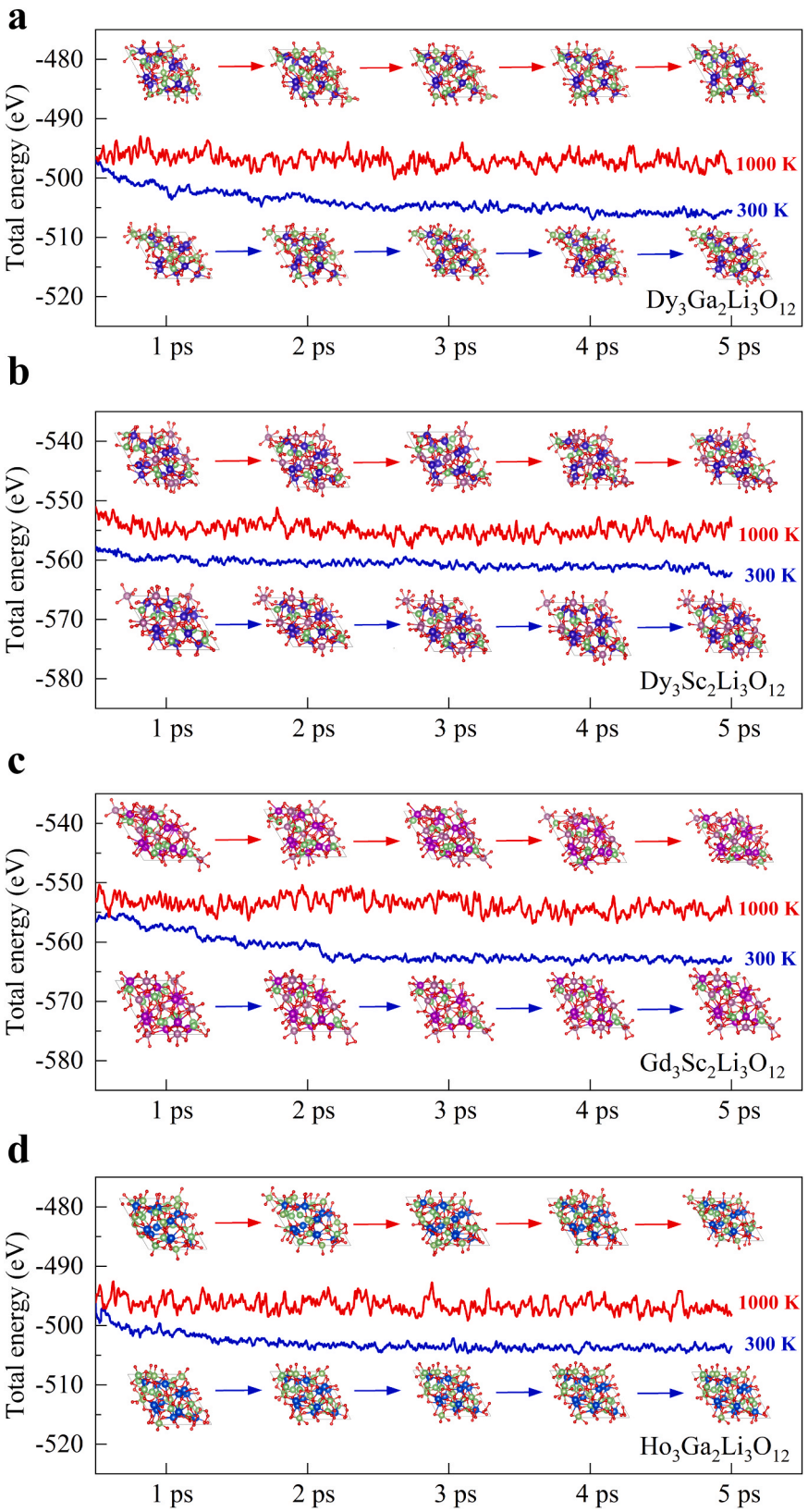

Fig. 8. Thermal dynamic stability evaluation at 300 K and 1000 K based on AIMD simulations. a $Dy_3Ga_2Li_3O_{12}$. b $Dy_3Sc_2Li_3O_{12}$. c $Gd_3Sc_2Li_3O_{12}$. d $Ho_3Ga_2Li_3O_{12}$. A total of 5000 fs of kinetics was performed for each system, with structures extracted at intervals of 2 fs.

species. More details of the CI-NEB method are provided in Note S3.

Code availability

The codes to construct XGB-*C* and XGB-*R* model in this study are available at: https://github.com//dmlc//xgboost.

CRediT authorship contribution statement

Zhilong Wang: Conceptualization, Methodology, Visualization, Data curation, Writing – original draft. **Yanqiang Han:** Methodology, Visualization. **Xirong Lin, Junfei Cai and Sicheng Wu:** Visualization, Data curation. **Xing Yu:** Writing – review & editing. **Jinjin Li:** Conceptualization, Methodology, Supervision, Resources, Writing – review & editing.

Declaration of Competing Interest

There are no conflicts of interest. J.J.L., Z.L.W., Y.Q.H., J.F.C. and S. C.W. have filed a patent related to this work: Chinese Application No. 202110260572.3, dated 10 March 2021.

Acknowledgements

The authors are grateful for the financial support provided by the National Natural Science Foundation of China (No. 21901157) and the National Key R&D Program of China (No. 2021YFC2100100).

Appendix A. Supporting information

Supplementary data associated with this article can be found in the online version at doi:10.1016/j.nanoen.2021.106337.

References

[1] J. Xie, Y.-C. Lu, A retrospective on lithium-ion batteries, Nat. Commun. 11 (2020) 2499.
[2] E. Fan, L. Li, Z. Wang, J. Lin, Y. Huang, Y. Yao, R. Chen, F. Wu, Sustainable recycling technology for Li-ion batteries and beyond: challenges and future prospects, Chem. Rev. 120 (2020) 7020–7063.
[3] S. Chen, F. Dai, M. Cai, Opportunities and challenges of high-energy lithium metal batteries for electric vehicle applications, ACS Energy Lett. 5 (2020) 3140–3151.
[4] M.T. McDowell, F.J.Q. Cortes, A.C. Thenuwara, J.A. Lewis, Toward high-capacity battery anode materials: chemistry and mechanics intertwined, Chem. Mater. 32 (2020) 8755–8771.
[5] X. Tian, Y. Yi, B. Fang, P. Yang, T. Wang, P. Liu, L. Qu, M. Li, S. Zhang, Design strategies of safe electrolytes for preventing thermal runaway in lithium ion batteries, Chem. Mater. 32 (2020) 9821–9848.
[6] H. Cha, et al., Boosting reaction homogeneity in high-energy lithium-ion battery cathode materials, Adv. Mater. 32 (2020), 2003040.
[7] S. Dou, et al., High-temperature shock enabled nanomanufacturing for energy-related applications, Adv. Energy Mater. 10 (2020), 2001331.
[8] Y. Liu, et al., 3D cube-maze-like Li-rich layered cathodes assembled from 2D porous nanosheets for enhanced cycle stability and rate capability of lithium-ion batteries, Adv. Energy Mater. 10 (2020), 1903139.
[9] C.F.J. Francis, I.L. Kyratzis, A.S. Best, Lithium-ion battery separators for ionic-liquid electrolytes: a review, Adv. Mater. 32 (2020), 1904205.
[10] H. Hong, J. Liu, H. Huang, C. Atangana Etogo, X. Yang, B. Guan, L. Zhang, Ordered macro–microporous metal–organic framework single crystals and their derivatives for rechargeable aluminum-ion batteries, J. Am. Chem. Soc. 141 (2019) 14764–14771.
[11] Z. Hu, H. Zhang, H. Wang, F. Zhang, Q. Li, H. Li, Nonaqueous aluminum ion batteries: recent progress and prospects, ACS Mater. Lett. 2 (2020) 887–904.
[12] S. Liu, et al., Nanomanufacturing of RGO-CNT hybrid film for flexible aqueous Al-ion batteries, Small 16 (2020), 2002856.
[13] C. Vaalma, D. Buchholz, M. Weil, S. Passerini, A cost and resource analysis of sodium-ion batteries, Nat. Rev. Mater. 3 (2018) 18013.
[14] T. Liu, et al., Sustainability-inspired cell design for a fully recyclable sodium ion battery, Nat. Commun. 10 (2019) 1965.
[15] C. Yang, S. Xin, L. Mai, Y. You, Materials design for high-safety sodium-ion battery, Adv. Energy Mater. 11 (2021), 2000974.
[16] Y. Liang, H. Dong, D. Aurbach, Y. Yao, Current status and future directions of multivalent metal-ion batteries, Nat. Energy 5 (2020) 646–656.
[17] S. Dey, J. Lee, S. Britto, J.M. Stratford, E.N. Keyzer, M.T. Dunstan, G. Cibin, S. J. Cassidy, M. Elgaml, C.P. Grey, Exploring cation–anion redox processes in one-dimensional linear chain vanadium tetrasulfide rechargeable magnesium ion cathodes, J. Am. Chem. Soc. 142 (2020) 19588–19601.
[18] Q. Zhao, S. Stalin, C.-Z. Zhao, L.A. Archer, Designing solid-state electrolytes for safe, energy-dense batteries, Nat. Rev. Mater. 5 (2020) 229–252.
[19] J.-F. Wu, et al., Inorganic solid electrolytes for all-solid-state sodium batteries: fundamentals and strategies for battery optimization, Adv. Funct. Mater. n/a (2020), 2008165.
[20] K.J. Kim, M. Balaish, M. Wadaguchi, L. Kong, J.L.M. Rupp, Solid-state Li–metal batteries: challenges and horizons of oxide and sulfide solid electrolytes and their interfaces, Adv. Energy Mater. 11 (2021), 2002689.
[21] A. Banerjee, X. Wang, C. Fang, E.A. Wu, Y.S. Meng, Interfaces and interphases in all-solid-state batteries with inorganic solid electrolytes, Chem. Rev. 120 (2020) 6878–6933.
[22] R. Chen, Q. Li, X. Yu, L. Chen, H. Li, Approaching practically accessible solid-state batteries: stability issues related to solid electrolytes and interfaces, Chem. Rev. 120 (2020) 6820–6877.
[23] Y. Zhu, et al., Lithium-film ceramics for solid-state lithionic devices, Nat. Rev. Mater. (2020).
[24] Y. Zhang, et al., Unsupervised discovery of solid-state lithium ion conductors, Nat. Commun. 10 (2019) 5260.
[25] F. Han, A.S. Westover, J. Yue, X. Fan, F. Wang, M. Chi, D.N. Leonard, N.J. Dudney, H. Wang, C. Wang, High electronic conductivity as the origin of lithium dendrite formation within solid electrolytes, Nat. Energy 4 (2019) 187–196.
[26] J.-F. Wu, X. Guo, Origin of the low grain boundary conductivity in lithium ion conducting perovskites: $Li_{3x}La_{0.67-x}TiO_3$, Phys. Chem. Chem. Phys. 19 (2017) 5880–5887.
[27] J.-F. Wu, X. Guo, Size effect in nanocrystalline lithium-ion conducting perovskite: $Li_{0.30}La_{0.57}TiO_3$, Solid State Ion. 310 (2017) 38–43.
[28] Y. Zhu, X. He, Y. Mo, Origin of outstanding stability in the lithium solid electrolyte materials: insights from thermodynamic analyses based on first-principles calculations, ACS Appl. Mater. Interfaces 7 (2015) 23685–23693.
[29] J.-F. Wu, W.K. Pang, V.K. Peterson, L. Wei, X. Guo, Garnet-type fast Li-ion conductors with high ionic conductivities for all-solid-state batteries, ACS Appl. Mater. Interfaces 9 (2017) 12461–12468.
[30] C. Wang, K. Fu, S.P. Kammampata, D.W. McOwen, A.J. Samson, L. Zhang, G. T. Hitz, A.M. Nolan, E.D. Wachsman, Y. Mo, V. Thangadurai, L. Hu, Garnet-type solid-state electrolytes: materials, interfaces, and batteries, Chem. Rev. 120 (2020) 4257–4300.
[31] J. Xu, et al., A garnet-type solid-electrolyte-based molten lithium−molybdenum−iron(II) chloride battery with advanced reaction mechanism, Adv. Mater. 32 (2020), 2000960.
[32] A.M. Nolan, Y. Zhu, X. He, Q. Bai, Y. Mo, Computation-accelerated design of materials and interfaces for all-solid-state lithium-ion batteries, Joule 2 (2018) 2016–2046.
[33] K.M. Jablonka, D. Ongari, S.M. Moosavi, B. Smit, Big-data science in porous materials: materials genomics and machine learning, Chem. Rev. 120 (2020) 8066–8129.
[34] A. Tkatchenko, Machine learning for chemical discovery, Nat. Commun. 11 (2020) 4125.
[35] S. Chen, M.R. Mahmoodi, Y. Shi, C. Mahata, B. Yuan, X. Liang, C. Wen, F. Hui, D. Akinwande, D.B. Strukov, M. Lanza, Wafer-scale integration of two-dimensional materials in high-density memristive crossbar arrays for artificial neural networks, Nat. Electron. 3 (2020) 638–645.
[36] J. Hermann, Z. Schätzle, F. Noé, Deep-neural-network solution of the electronic Schrödinger equation, Nat. Chem. 12 (2020) 891–897.
[37] K. Muraoka, Y. Sada, D. Miyazaki, W. Chaikittisilp, T. Okubo, Linking synthesis and structure descriptors from a large collection of synthetic records of zeolite materials, Nat. Commun. 10 (2019) 4459.
[38] Z. Wang, H. Zhang, J. Li, Accelerated discovery of stable spinels in energy systems via machine learning, Nano Energy 81 (2021), 105665.
[39] G. Pesciullesi, P. Schwaller, T. Laino, J.-L. Reymond, Transfer learning enables the molecular transformer to predict regio- and stereoselective reactions on carbohydrates, Nat. Commun. 11 (2020) 4874.
[40] Z. Wang, et al., Predicting adsorption ability of adsorbents at arbitrary sites for pollutants using deep transfer learning, npj Comput. Mater. 7 (2021) 19.
[41] Z. Wang, Q. Wang, Y. Han, Y. Ma, H. Zhao, A. Nowak, J. Li, Deep learning for ultra-fast and high precision screening of energy materials, Energy Storage Mater. 39 (2021) 45–53.
[42] Y.-T. Chen, M. Duquesnoy, D.H.S. Tan, J.M. Doux, H. Yang, G. Deysher, P. Ridley, A.A. Franco, Y.S. Meng, Z. Chen, Fabrication of high-quality thin solid-state electrolyte films assisted by machine learning, ACS Energy Lett. 6 (2021) 1639–1648.
[43] Y. Wang, T. Xie, A. France-Lanord, A. Berkley, J.A. Johnson, Y. Shao-Horn, J. C. Grossman, Toward designing highly conductive polymer electrolytes by machine learning assisted coarse-grained molecular dynamics, Chem. Mater. 32 (2020) 4144–4151.
[44] Q. Zhao, M. Avdeev, L. Chen, S. Shi, Machine learning prediction of activation energy in cubic Li-argyrodites with hierarchically encoding crystal structure-based (HECS) descriptors, Sci. Bull. (2021).
[45] A. Jain, et al., Commentary: the materials project: a materials genome approach to accelerating materials innovation, APL Mater. 1 (2013), 011002.
[46] G. Henkelman, B.P. Uberuaga, H. Jónsson, A climbing image nudged elastic band method for finding saddle points and minimum energy paths, J. Chem. Phys. 113 (2000) 9901–9904.
[47] Z. Song, D. Zhou, Q. Liu, Tolerance factor and phase stability of the garnet structure, Acta Cryst. C 75 (2019) 1353–1358.

[48] V. Gladkikh, D.Y. Kim, A. Hajibabaei, A. Jana, C.W. Myung, K.S. Kim, Machine learning for predicting the band gaps of ABX_3 perovskites from elemental properties, J. Phys. Chem. C 124 (2020) 8905–8918.
[49] V. Thangadurai, D. Pinzaru, S. Narayanan, A.K. Baral, Fast solid-state Li ion conducting garnet-type structure metal oxides for energy storage, J. Phys. Chem. Lett. 6 (2015) 292–299.
[50] T. Asano, et al., Solid halide electrolytes with high lithium-ion conductivity for application in 4 V class bulk-type all-solid-state batteries, Adv. Mater. 30 (2018), 1803075.
[51] X. Li, J. Liang, N. Chen, J. Luo, K.R. Adair, C. Wang, M.N. Banis, T.K. Sham, L. Zhang, S. Zhao, S. Lu, H. Huang, R. Li, X. Sun, Water-mediated synthesis of a superionic halide solid electrolyte, Angew. Chem. Int. Ed. 58 (2019) 16427–16432.
[52] J. Qiu, et al., Enabling stable cycling of 4.2 V high-voltage all-solid-state batteries with PEO-based solid electrolyte, Adv. Funct. Mater. 30 (2020), 1909392.
[53] J. Schnell, F. Tietz, C. Singer, A. Hofer, N. Billot, G. Reinhart, Prospects of production technologies and manufacturing costs of oxide-based all-solid-state lithium batteries, Energy Environ. Sci. 12 (2019) 1818–1833.
[54] M. Liu, A. Jain, Z. Rong, X. Qu, P. Canepa, R. Malik, G. Ceder, K.A. Persson, Evaluation of sulfur spinel compounds for multivalent battery cathode applications, Energy Environ. Sci. 9 (2016) 3201–3209.
[55] Z. Zhang, Y. Shao, B. Lotsch, Y.S. Hu, H. Li, J. Janek, L.F. Nazar, C.W. Nan, J. Maier, M. Armand, L. Chen, New horizons for inorganic solid state ion conductors, Energy Environ. Sci. 11 (2018) 1945–1976.
[56] J. Lee, N. Ohba, R. Asahi, Design rules for high oxygen-ion conductivity in garnet-type oxides, Chem. Mater. 32 (2020) 1358–1370.
[57] H. Park, Y. Lee, M. Cho, J. Kang, W. Ko, Y.H. Jung, T.Y. Jeon, J. Hong, H. Kim, S. T. Myung, J. Kim, $Na_2Fe_2F_7$: a fluoride-based cathode for high power and long life Na-ion batteries, Energy Environ. Sci. 14 (2021) 1469–1479.
[58] A. Hayashi, K. Minami, F. Mizuno, M. Tatsumisago, Formation of Li^+ superionic crystals from the Li_2S–P_2S_5 melt-quenched glasses, J. Mater. Sci. 43 (2008) 1885–1889.
[59] N. Kamaya, K. Homma, Y. Yamakawa, M. Hirayama, R. Kanno, M. Yonemura, T. Kamiyama, Y. Kato, S. Hama, K. Kawamoto, A. Mitsui, A lithium superionic conductor, Nat. Mater. 10 (2011) 682–686.
[60] S. Hori, S. Taminato, K. Suzuki, M. Hirayama, Y. Kato, R. Kanno, Structure–property relationships in lithium superionic conductors having a $Li_{10}GeP_2S_{12}$-type structure, Acta Crystallogr. Sect. B Struct. Sci. Cryst. Eng. Mater. 71 (2015) 727–736.
[61] Y. Kato, et al., High-power all-solid-state batteries using sulfide superionic conductors, Nat. Energy 1 (2016) 16030 (s).
[62] Chen, T., Guestrin, C. XGBoost. Proceedings of the 22nd ACM SIGKDD International Conference on Knowledge Discovery and Data Mining (2016).
[63] G. Kresse, J. Furthmüller, Efficient iterative schemes for ab initio total-energy calculations using a plane-wave basis set, Phys. Rev. B 54 (1996) 11169–11186.
[64] P.E. Blöchl, Projector augmented-wave method, Phys. Rev. B 50 (1994) 17953–17979.
[65] G. Kresse, D. Joubert, From ultrasoft pseudopotentials to the projector augmented-wave method, Phys. Rev. B 59 (1999) 1758–1775.
[66] J.P. Perdew, K. Burke, M. Ernzerhof, Generalized gradient approximation made simple, Phys. Rev. Lett. 77 (1996) 3865–3868.
[67] S. Nosé, A unified formulation of the constant temperature molecular dynamics methods, J. Chem. Phys. 81 (1984) 511–519.
[68] W.G. Hoover, Canonical dynamics: equilibrium phase-space distributions, Phys. Rev. A 31 (1985) 1695–1697.
[69] M.A. Green, Intrinsic concentration, effective densities of states, and effective mass in silicon, J. Appl. Phys. 67 (1990) 2944–2954.
[70] X. He, Y. Zhu, A. Epstein, Y. Mo, Statistical variances of diffusional properties from ab initio molecular dynamics simulations, npj Comput. Mater. 4 (2018) 18.